Computational Materials Science 211 (2022) 111500

Contents lists available at ScienceDirect

Computational Materials Science

journal homepage: www.elsevier.com/locate/commatsci

Full length article

Ab initio morphology prediction of Zr hydride precipitates using atomistically informed Eshelby's ellipsoidal inclusion

Akio Ishii

Department of Mechanical Science and Bioengineering, Osaka University, 1-3 Machikaneyama, Toyonaka, Osaka 560-8531, Japan

ARTICLE INFO

Keywords:
Zirconium hydride
Micromechanics
Eshelby's ellipsoidal inclusion
Atomistic simulation
Density functional theory

ABSTRACT

We energetically predicted the morphology of Zr hydride precipitates in a hexagonal close-packed (HCP) Zr matrix. Considering Zr hydride precipitates as ellipsoids, we used Eshelby's ellipsoidal inclusions to calculate the elastic energy increment due to the presence of Zr hydride precipitates in the Zr matrix, in which the elastic anisotropy and inhomogeneity of the elastic constants between Zr and Zr hydride were considered. We compared the difference in the elastic energy increment between the ellipsoidal inclusions with different shapes: plates (mimicked by penny-shape ellipsoids), needles (mimicked by longitudinal ellipsoids) and sphere, and orientations to detect the stable structure with the minimum elastic energy increment. Eigenstrains of each Zr hydride and elastic constants of Zr hydrides and HCP Zr for Eshelby's ellipsoidal inclusion analysis were determined using atomistic simulations based on a density functional theory calculation, achieving a parameter free *ab initio* morphology prediction. The morphology predictions were implemented for two cases: with and without shear components of eigenstrain ($w/$ and w/o shear). The $\langle 1\bar{2}10\rangle$ longitudinal needle for the γ hydride (w/o shear) and plate (or disk) on the plane, which is 20° to 30° tilted about $\langle 1\bar{2}10\rangle$-axis from basal plane (0001), for δ and ϵ hydrides ($w/$ shear) were successfully predicted as stable shapes and orientations of the precipitates under zero external stress conditions, qualitatively consistent with experimental observations. The external circumferential tensile stress on the basal plane reduces the elastic energy of [0001] parallel Zr hydride plates, which is also qualitatively consistent with the reoriented δ hydride precipitates observed in the experiment. On the other hand, predicted external stress for the reorientation of Zr hydride is quite high, around 10 GPa. This is inconsistent with experimental observation and further investigation is necessary. Generally, our predictions based on elasticity theory appear qualitatively consistent with experimental observations, suggesting an elastic origin of the morphology of Zr hydride precipitates in the HCP Zr matrix.

1. Introduction

Zr alloys are commonly used as fuel cladding in nuclear reactors because of their desirable properties: low cross-section for neutron absorption, good corrosion resistance in steam-water conditions, and sufficient ductility and fracture toughness. Because the Zr fuel cladding is constantly exposed to steam-water in a nuclear reactor, hydrogen generates due to the oxidation of Zr surface. Some part of generated hydrogen is absorbed by the Zr fuel cladding. Once the hydrogen concentration in the Zr fuel cladding exceeds the limit of solid solubility, Zr hydride precipitates are easily generated [1,2]. From experimental studies, it is known that Zr hydride precipitates have a negative effect on the mechanical properties of Zr alloys. The reduction in the ductility and fracture toughness of Zr alloys due to Zr hydride has been experimentally observed, and it has been reported that the reduction is related to the morphology, i.e. shape and orientation, of Zr hydride precipitates [2–5].

The experimentally observed Zr hydride precipitates are ζ (Zr_2H), γ (ZrH), δ ($ZrH_{1.66}$), and ϵ (ZrH_2) hydrides, which have extremely similar crystalline structures: face-centered tetragonal (FCT) for ζ, γ and ϵ hydrides, face-centered cubic (FCC) for δ hydrides [1,3,6], whereas the matrix is hexagonal closed-packed (HCP) Zr (α Zr). Most commonly observed hydrides are γ and δ. A $\langle 1\bar{2}10\rangle$ longitudinal needle shape was observed as the shape and orientation of the γ hydride precipitate [7,8]. A nano-scale plate (or disk) shape on the basal plane (0001) precipitate is observed for δ hydride and it was reported that these plate shape precipitates construct a "deck of cards" structure with several tilts about the $\langle 1\bar{2}10\rangle$-axis [1,2]. Furthermore, for a δ hydride, micro-scale "deck of cards" clusters along the parallel $\langle 0001\rangle$ direction during cooling was also observed under loading conditions [9–11]. This is often called as the reorientation of Zr hydrides and researchers revealed that this reorientation drastically reduced the fracture toughness of Zr

E-mail address: ishii@me.es.osaka-u.ac.jp.

https://doi.org/10.1016/j.commatsci.2022.111500
Received 13 February 2022; Received in revised form 30 April 2022; Accepted 5 May 2022
Available online 19 May 2022

alloys [12–14]. In contrast, around hydride precipitates, complex bird-nest-shaped dislocation structures are frequently observed [8,15–17], suggesting that the hydride precipitates drive the surrounding dislocation emission. This could be considered as a type of chemomechanical effect; hydride precipitates, which are the products of the chemical reaction between Zr and H, activate plastic deformation.

Owing to the importance of the Zr hydride structures, theoretical studies on the shape, orientation, and surrounding dislocation of Zr hydride precipitates have been performed [18–24]. E.g., Han *et al*. successfully reproduced the above "deck of cards" shape precipitate and reorientation effect under tensile stress conditions for δ hydride precipitates, using a phase-field simulation considering the anisotropy of interface energy [22]. On the other hand, Simon *et al*. reported the effect of applied stress is not significant for the reorientation of δ hydride in a single crystal and questioned the mechanisms behind reorientation very recently using phase field simulation, making the discussion controversial [25]. Tummala *et al*. reproduced complex dislocation structures around the Zr hydride precipitate and revealed the correlation between the nucleation of dislocations and subsequent hydride precipitates using dislocation dynamics simulation [21].

Despite these recent efforts and successes in meso-scale simulation, several aspects remain to be clarified, for example, why the morphology of each Zr hydride is different; γ hydride precipitates have a needle structure and δ hydride precipitates have a plate structure. The origin of the stable shape and orientation of Zr hydride precipitates remains controversial, and there is a lack of atomistic and electronic information to guarantee the quality of the microscopic physics of the meso-scale simulation [26]. Although considerable atomistic analyses have been conducted for Zr hydrides using empirical or density functional theory (DFT) interatomic potentials [6,27–34], the connection between atomic-scale and meso-scale analyses is weak.

In this study, we theoretically predict the morphology of γ, δ, and ϵ hydride precipitates in an HCP Zr matrix (α Zr) under zero and tensile stress conditions. We use Eshelby's ellipsoidal inclusions to calculate the elastic energy increment due to the presence of Zr hydride precipitates in the Zr matrix, in which the elastic anisotropy and inhomogeneity of the elastic constants between HCP Zr and Zr hydride were considered. We compare the difference in elastic energy increment between the ellipsoidal inclusions with different shapes (sphere, disk, and needle) and their orientations. The eigenstrains of each Zr hydride and the elastic constants of Zr hydrides and HCP Zr for Eshelby's ellipsoidal inclusion analysis were obtained using atomistic simulation with a DFT calculation, achieving a parameter free *ab initio* morphology prediction. This is an advantage of our method compared with previous meso-scale analysis, which usually includes empirical parameters or descriptions.

2. Method

2.1. Micromechanics theory and Eshelby's ellipsoidal inclusions

When an elastic medium (referred to as a matrix in this study) is distorted by regional dimensional changes due to plastic flow, phase transformation, and thermal expansion, an internal stress field appears within and outside the deformed region. These dimensional changes are usually described as a strain form, which is called the eigenstrain in micromechanics theory. Using the distribution of the eigenstrains, $\epsilon_{ij}(\boldsymbol{x})$ ($\boldsymbol{x}$ indicates the position inside the matrix), we can calculate the distribution of the displacement $u_k(\boldsymbol{x})$ and total strains inside the inclusion $\varepsilon_{kl}(\boldsymbol{x}) = \frac{\partial u_k}{\partial x_l}$ by solving the following differential equation, described using Einstein summation convention [35],

$$C_{ijkl}\frac{\partial^2 u_k(\boldsymbol{x})}{\partial x_l \partial x_j} = C_{ijkl}\frac{\partial \epsilon_{kl}(\boldsymbol{x})}{\partial x_j}. \tag{1}$$

Where C_{ijkl} are elastic constants. Once the total strains ε_{kl} are calculated, the distribution of the internal stress $\sigma_{ij}(\boldsymbol{x})$ is derived as follows:

$$\sigma_{ij}(\boldsymbol{x}) = C_{ijkl}(\varepsilon_{kl}(\boldsymbol{x}) - \epsilon_{kl}(\boldsymbol{x})). \tag{2}$$

Here $(\varepsilon_{kl}(\boldsymbol{x}) - \epsilon_{kl}(\boldsymbol{x}))$ are the distribution of elastic strains. In recent studies, the differential Eq. (1) is usually used as the stress solver in the phase-field method, and is solved numerically with a fast Fourier transform algorithm [22,26,36,37].

Likewise, Eshelby stated that the total strains and eigenstrains are linearly connected with Eshelby's tensor, S_{klmn}, if we consider the deformed region as an ellipsoidal inclusion ($\frac{x_1^2}{a_1^2} + \frac{x_2^2}{a_2^2} + \frac{x_3^2}{a_3^2} = 1$: a_i is the half axis of the ellipsoid in each direction) as Zr hydride precipitates [38,39], and the eigenstrains distribute uniformly in the inclusion.

$$\varepsilon_{kl} = S_{klmn}\epsilon_{mn}. \tag{3}$$

In the isotropic matrix, S_{klmn} depends only on Poisson's ratio and the shape of the ellipsoidal inclusion, independent of the volume. If the eigenstrains ϵ_{mn} and Eshelby's tensor S_{klmn} are known, the internal stress of the ellipsoidal inclusion σ_{ij} is derived from Eqs. (2) and (3). Using the derived σ_{ij}, the elastic energy increment ΔE (per unit volume of inclusion) owing to the inclusion in the matrix under external stress $\sigma_{ij}^{\mathrm{ex}}$ condition, is described as follows [35]:

$$\Delta E = -\frac{1}{2}\sigma_{ij}\epsilon_{ij} - \sigma_{ij}^{\mathrm{ex}}\epsilon_{ij}. \tag{4}$$

Comparing the elastic energy increment ΔE between the inclusions with different shapes and orientations, we can predict the stable shape and orientation for the inclusion with the minimum energy increment. However, because the external stress term on the right side is independent of the shape of the inclusion, there is no elastic energy increment owing to the correlation between the external stress and the shape (or orientation) of the inclusion. Thus, in this case, we cannot consider the external stress effect on the morphology change of inclusions, as the researchers observed in the experiment for Zr hydride precipitates [9–11].

If the elastic constants are not uniform in the matrix ($C_{ijkl} = C_{ijkl}(\boldsymbol{x})$), for example, the deformed region (or inclusion) has different elastic constants from the original matrix owing to differences in the atomic structure, such as FCT (or FCC) Zr hydride (inclusion) and HCP Zr (matrix) case, solving Eq. (1) is usually difficult. Fortunately, Eshelby also stated that there is a relationship between the elastic constants of matrix C_{ijkl}, that of inclusion $\tilde{C}_{ijkl}$ and fictitious eigenstrains $\tilde{\epsilon}_{mn}$ based on his "equivalent inclusion theory" for the ellipsoidal inclusion [35,39],

$$\tilde{C}_{ijkl}(S_{klmn}\tilde{\epsilon}_{mn} - \epsilon_{kl}) = C_{ijkl}(S_{klmn}\tilde{\epsilon}_{mn} - \tilde{\epsilon}_{kl}). \tag{5}$$

This equation is derived from the concept that the inclusion with different elastic constants from the matrix is replaced with a fictitious inclusion with the same elastic constants as the matrix but with additional fictitious eigenstrains (equivalent inclusion). The left and right sides of this equation are derived from Eq. (2) for the real and fictitious inclusion, respectively, and the total strains term are described using fictitious eigenstrains $\tilde{\epsilon}_{mn}$ as $\varepsilon_{kl} = S_{klmn}\tilde{\epsilon}_{mn}$. Solving these simultaneous equations for $\tilde{\epsilon}_{mn}$ and calculating σ_{ij} using Eq. (2), the elastic energy increment, $\Delta\tilde{E}$, owing to the inclusion in the matrix under external stress $\sigma_{ij}^{\mathrm{ex}}$ condition, is rewritten as follows [35]:

$$\Delta\tilde{E} = -\frac{1}{2}\sigma_{ij}\epsilon_{ij} - \sigma_{ij}^{\mathrm{ex}}\epsilon_{ij} - \frac{1}{2}\sigma_{ij}^{\mathrm{ex}}(\tilde{\epsilon}_{ij} - \epsilon_{ij}). \tag{6}$$

In contrast to Eq. (4), the third term on the right side is a correlation term between the external stress and the shape and orientation of the inclusion because $\tilde{\epsilon}_{ij}$ are shape and orientation dependent. Thus, in this case, the effect of external stress on the morphology change was considered. Although the original Eshelby tensor applies for an

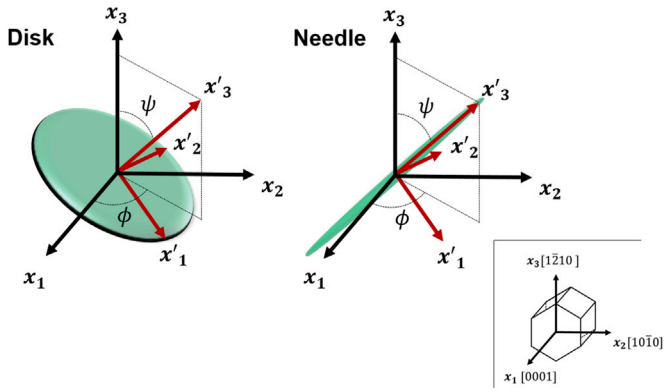

Fig. 1. Definition of the x coordinates of the matrix and the x' coordinates of the disk and needle inclusions. The x'_3 axis is chosen to be perpendicular to the disk and parallel to the longitude of the needle. Disk and needle inclusions are mimicked by penny-shape and longitudinal ellipsoids in this study.

isotropic matrix and inclusion, the general form of Eshelby's tensor for anisotropic matrix and inclusion (such as HCP Zr and FCT (or FCC) Zr hydride) is also derived as follows based on Kinoshita *et al*.'s deduction [24,35,40]:

$$S^*_{klmn} = \frac{1}{8\pi} C_{pqmn} \int_{-1}^{1} d\zeta_3 \times \int_0^{2\pi} \left(\frac{\xi_l \xi_q N_{kp}(\xi_1,\xi_2,\xi_3) + \xi_k \xi_q N_{lp}(\xi_1,\xi_2,\xi_3)}{D(\xi_1,\xi_2,\xi_3)} \right) d\theta, \tag{7}$$

where

$$D(\xi_1,\xi_2,\xi_3) = P_{pqr}(C_{pj1l}\xi_j\xi_l)(C_{qm2n}\xi_m\xi_n)(C_{rs3t}\xi_s\xi_t),$$
$$N_{km}(\xi_1,\xi_2,\xi_3) = \frac{1}{2} P_{ksl} P_{mnr}(C_{sjnl}\xi_l\xi_j)(C_{turv}\xi_u\xi_v),$$

which correspond to the determinant and cofactor of $K_{km} = C_{klmn}\xi_l\xi_n$, respectively. P_{pqr} denotes the permutation tensor. Using ζ_3 and θ, $[\xi_1;\xi_2;\xi_3]$ are described as follows:

$$\begin{bmatrix} \xi_1 \\ \xi_2 \\ \xi_3 \end{bmatrix} = \begin{bmatrix} \frac{\sqrt{1-\zeta_3^2}\cos\theta}{a_1} \\ \frac{\sqrt{1-\zeta_3^2}\sin\theta}{a_2} \\ \frac{\zeta_3}{a_3} \end{bmatrix}$$

In this study, considering HCP Zr and Zr hydride precipitates as a matrix and inclusions, respectively, we numerically calculated the anisotropic Eshelby's tensor using Eq. (7). Then, using Eqs. (5), (2), and (6), we calculated the elastic energy increment $\Delta\tilde{E}$ for different shapes and orientations of the Zr hydride precipitate, which includes the effect of elastic anisotropy and inhomogeneity between HCP Zr and FCT Zr hydrides. By comparing the $\Delta\tilde{E}$ value of Zr hydride precipitates with different shapes and orientations, we energetically predicted the stable shape and orientation of the Zr hydride precipitate with the minimum $\Delta\tilde{E}$ value. Using the elastic constant values of the HCP Zr matrix (C_{ijkl}), that of Zr hydride ($\tilde{C}_{ijkl}$), and eigenstrain values of Zr hydride (ϵ_{mn}), which are obtained from atomistic simulations with DFT calculation, we achieved a parameter free *ab initio* prediction.

Following previous studies using Eshelby's tensor [24,35,41], we only considered spheres, disks (mimicked by penny-shape ellipsoids) and needles (mimicked by longitudinal ellipsoids) as the shape of the Zr hydride precipitate for simplicity. Note recent phase field study's observed more complicated shape of Zr hydride inclusion, saddle-like shape [25], that is out of the range of Eshelby's inclusion analysis. For the orientation of disk and needle shape Zr hydrides, using following rotation matrix

$$R_{ij} = \begin{bmatrix} \cos\psi & 0 & -\sin\psi \\ 0 & 1 & 0 \\ \sin\psi & 0 & \cos\psi \end{bmatrix} \times \begin{bmatrix} \cos\phi & \sin\phi & 0 \\ -\sin\phi & \cos\phi & 0 \\ 0 & 0 & 1 \end{bmatrix} = \begin{bmatrix} \cos\psi\cos\phi & \cos\psi\sin\phi & -\sin\psi \\ -\sin\phi & \cos\phi & 0 \\ \sin\psi\cos\phi & \sin\psi\sin\phi & \cos\psi \end{bmatrix}, \tag{8}$$

we describe the elastic constants and eigenstrains in the coordinate system x' of the rotated disk and needle inclusions, as shown in Fig. 1. The normal direction of the disk plane and the longitudinal direction of the needle were set to x'_3. We then calculated the orientation-dependent Eshelby's tensor and elastic energy increment by changing the rotation angle (ϕ,ψ) from 0° to 180° per 10°. Although the disk and needle are considered as shapes with an extremely long and short half axes of inclusion analytically (e.g., $a_1 = a_2$ and $a_3/a_1 \to 0$ for disk, $a_3/a_1 \to \infty$ for needle) [35,41], we consider $(a_1;a_2;a_3) = (10/\sqrt{2};10/\sqrt{2};1)$ and $(a_1;a_2;a_3) = (1;1;10)$ ellipsoid as disk and needle inclusions, respectively, in this study, because of limitations to the numerical calculations. Note that determining a unit for the half axes is unnecessary, as Eshelby's tensor is independent of the inclusion volume. Additionally, we have to mention, although the ratio between the half-axes of the precipitates are fixed to certain values in our study, we confirmed the effect of it is ignorable; the setting: $(a_1;a_2;a_3) = (20/\sqrt{2};20/\sqrt{2};1)$ disk and $(a_1;a_2;a_3) = (1;1;20)$ needle gives almost same results as the present setting.

As previously mentioned, phase-field type studies, using Eq. (1) from micromechanics as the stress solver is the main driving horse behind recent morphological studies in the materials science field [22,26,36,37,42,43]. Compared with conventional studies, the merit of using Eshelby's tensor is that we can reduce the computation cost, and we need not consider boundary (or size) effects and resolution of the matrix system in the simulation. To avoid empirical or ambiguous description in our model as possible, we do not consider the effect of chemical interface energy in our method. Although recent phase-field simulations consider the chemical interface energy [22,25], we think they include empirical or ambiguous description (or assumption) more or less about it and the anisotropic chemical interface energy is not fully considered. This is because including the non-linearly orientation-dependent chemical interface energy solidly in the meso-scale model is usually difficult. Once the non-linearly orientation-dependent chemical interface energy is informed accurately to our method from DFT atomistic simulation, e.g., using recent high performance super computer, more practical morphology predication is possible, considering the anisotropic chemical interface energy. Note, if the size of inclusion is enough large, usually larger than micro-scale, the chemical interface energy is ignorable because the elastic energy is volume-dependent and chemical interface energy is (surface) area-dependent. E.g., the elastic energy increment is usually of the order of GJ/m^3 and the chemical interface energy is of the order of J/m^2, roughly we can say the chemical interface energy is 1000 times smaller than the elastic energy increment for the micro-scale inclusion. On the other hand, the order of both energies become the same at nano-scale.

Additionally, nano-scale Zr hydride precipitates construct micro-scale clusters as we mentioned above. Because Eshelby's tensor is scale free, we think our method is applicable for these clusters considering the cluster itself as one inclusion. Although the mixture effect of Zr matrix and hydrides exists; eigenstrain and elastic constants should be averaged ones as a single inclusion, we confirmed the effects does not change the morphology prediction of the Zr hydrides in this study.

2.2. Atomistic informed eigenstrains of Zr hydride precipitate

Next, we explain the method for calculating the eigenstrains of Zr hydrides using atomistic simulations. Let us consider the phase transformation process from HCP Zr to FCT (or FCC) Zr hydride. As in Fig. 2,

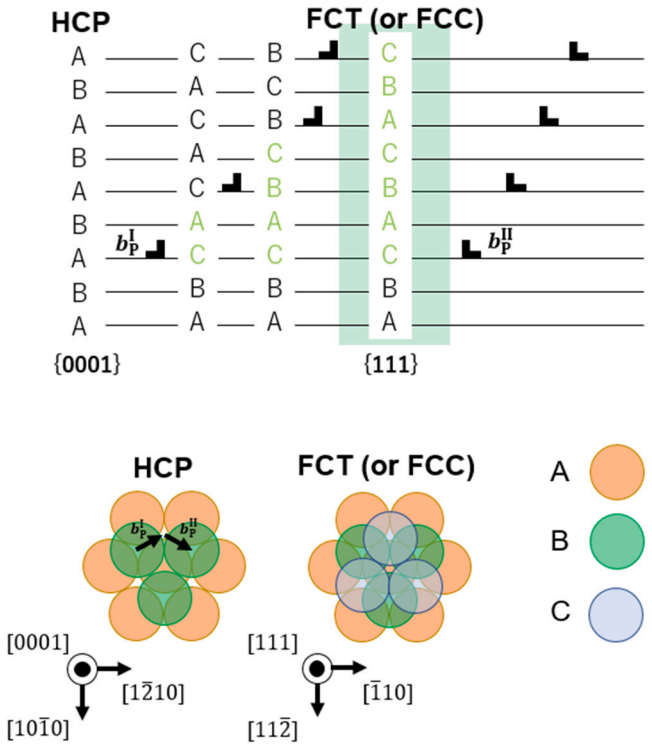

Fig. 2. The relationship between the Shockley partial dislocations ($\boldsymbol{b}_P^I, \boldsymbol{b}_P^{II}$) in HCP structure and the atomic layer stacking sequences of HCP and FCT (or FCC) structures.

HCP structures have a ABABAB… basal stacking sequence whereas FCT (or FCC) phase structures have a ABCABC… {111} stacking sequence. The FCT ABCABC… {111} stacking sequence can be considered as an HCP ABABAB… basal stacking sequence with basal plane stacking faults at every other basal plane. The in-basal-plane HCP-FCT phase boundary along the [10$\bar{1}$0] direction can be described as a set of Shockley partial dislocations, $\boldsymbol{b}_P^I = 1/3\langle 10\bar{1}0\rangle$ or $\boldsymbol{b}_P^{II} = 1/3\langle 01\bar{1}0\rangle$, located at every other basal plane. Thus, if the FCT phase is spontaneously precipitated in the HCP phase, the phase transformation may generate an engineering shear strain, $b_P^I/(4d)$ in the $\langle 10\bar{1}0\rangle$ direction on the basal plane, where d is the inter-basal-plane distance. The result of FCT (or FCC) Zr in this process is satisfied with the experimentally observed orientation relationship between the FCT (or FCC) Zr hydride and HCP Zr matrix: $(111)_{FCT}//(0001)_{HCP}$ and $\langle 110\rangle_{FCT}$ $\langle 1\bar{2}10\rangle_{HCP}$ [7].

From this crystallographic relationship between HCP and FCT (or FCC), we consider an FCT (or FCC) Zr supercell that is obtained by shearing the HCP Zr supercell, applying $\boldsymbol{b}_P^I$, as shown in Fig. 3. We then charge H atoms to the FCT Zr supercell to compute the eigenstrains in the H-charged FCT ZrH and ZrH_2 supercells, which represent γ and ϵ hydrides, respectively. We used a two-atom supercell for HCP Zr and FCT ZrH_2 computation and a double-sized four-atom supercell of FCT Zr for ZrH computation to describe its stable H's site occupation (see Fig. 3). In the FCT (or FCC) Zr, DFT studies have revealed that H atoms prefer to occupy the tetragonal site (T-site) [6] and the most energetically stable H arrangement at 0 K, in which all of the H atoms are placed on almost linearly aligned T-sites on the {110} plane for ZrH and all T-sites in FCT are occupied by H atoms for ZrH_2 [6,27]. Therefore, we simply employ these H arrangements by inserting four H atoms into the T-sites in the four-atom and two-atom Zr supercell for ZrH and ZrH_2, respectively. Here, the finite-temperature entropic effects, such as the H configuration and atomic vibration entropies, are ignored. We optimized the supercell shape and atomic structure of the HCP Zr supercell and ZrH and ZrH_2 supercells, and obtained optimized supercell matrices: $\boldsymbol{H}_{\mathbf{HCP}} = [\boldsymbol{h}_1^{\mathbf{HCP}}\ \boldsymbol{h}_2^{\mathbf{HCP}}\ \boldsymbol{h}_3^{\mathbf{HCP}}]$ for HCP Zr supercell and $\boldsymbol{H}_{\mathbf{ZrH}} = [\boldsymbol{h}_1^{\mathbf{ZrH}}\ 0.5\boldsymbol{h}_2^{\mathbf{ZrH}}\ \boldsymbol{h}_3^{\mathbf{ZrH}}]$, $\boldsymbol{H}_{\mathbf{ZrH_2}} = [\boldsymbol{h}_1^{\mathbf{ZrH_2}}\ \boldsymbol{h}_2^{\mathbf{ZrH_2}}\ \boldsymbol{h}_3^{\mathbf{ZrH_2}}]$ for ZrH and ZrH_2 supercells respectively. The eigenstrains ϵ_{ij}^X for Zr hydrides can be computed using the supercell matrices in the form of Green strain as

$$\epsilon_{ij}^X = \frac{1}{2}(\boldsymbol{J}_{\mathbf{X}}^T\boldsymbol{J}_{\mathbf{X}} - \boldsymbol{I}), \tag{9}$$

where $\boldsymbol{J}_{\mathbf{X}}^T = \boldsymbol{H}_{\mathbf{X}}\left(\boldsymbol{H}_{\mathbf{HCP}}\right)^{-1}$ is the deformation tensor, and the subscript X is ZrH or ZrH_2. To perform the DFT structural optimizations, we used the VASP computational package [44]. The electron-ion interaction in the DFT is described using the projector-augmented wave method [45]. The exchange–correlation between electrons is treated using the Perdew–Wang generalized gradient approximation in the PW91 functional [46], and the energy cutoff is 290 eV for the plane-wave basis set. The energy convergence criteria of the electronic and ionic structure relaxations were set to 1.0×10^{-8} and 1.0×10^{-4} eV, respectively. A 13 × 13 × 13 k-point mesh was used for HCP Zr and ZrH_2. A 13 × 7 × 13 k-point mesh was used for the ZrH. We confirmed the convergence of eigenstrains and elastic constants with respect to the above DFT input parameters. Although atomistic simulation with DFT calculation (0 K) indicates that the most stable Zr hydride is ZrH_2 (ε hydride) [6], $ZrH_{1.66}$ (δ hydride, FCC structure) was the most frequently observed in experiments [1,47]. Unfortunately, extensive details regarding the H atom arrangements in $ZrH_{1.66}$ is still unclear, and theoretical studies using atomistic simulation is computationally expensive and time consuming due to the very large supercell structure. Thus, we approximate the elastic constants and eigenstrains of $ZrH_{1.66}$ by simple linear interpolation between those of ZrH and ZrH_2 in this study.

$$\begin{aligned} C_{ijkl}^{ZrH_{1+x}} &= (1-x)C_{ijkl}^{ZrH} + xC_{ijkl}^{ZrH_2}, \\ \epsilon_{ij}^{ZrH_{1+x}} &= (1-x)\epsilon_{ij}^{ZrH} + x\epsilon_{ij}^{ZrH_2}, \end{aligned} \tag{10}$$

and $x = 0.66$.

Each component of the calculated eigenstrain ϵ_{ij}^X is listed in Table 1. For the comparison, the eigenstrains calculated from the simple lattice correspondence between HCP and FCT (for the detail, please refer the appendix), using previous reported lattice constants, are also included. In addition to the basal shear along [10$\bar{1}$0], ϵ_{12}, a large normal and parallel expansion to the basal plane appears: ϵ_{11}, ϵ_{22} for ZrH, and ϵ_{33} for ZrH_2, which is consistent with the eigenstrains calculated using previous results though ϵ_{11}, ϵ_{22} and ϵ_{12} for ZrH are larger and ϵ_{12} for ZrH_2 are smaller. The calculated normal components of the eigenstrain of $ZrH_{1.66}$ are almost transversely isotropic for the basal plane, which is also consistent with previous result. We also confirmed that these eigenstrains change the c/a ratio of the supercell of HCP Zr to 1.63 approximately, indicating that the shape of the supercell is cubic. The elastic constants of HCP Zr, ZrH, $ZrH_{1.66}$ and ZrH_2 are listed in Table 2. That of HCP Zr, ZrH and ZrH_2 are calculated by computing the Hessian matrix using the supercells of HCP Zr, ZrH, and ZrH_2, respectively [48,49]. For the comparison, the elastic constants, that were reported in previous studies, are also included. Calculated elastic constants are generally consistent with previous results. Note elastic constants in Table 2 are defined in $[111](\boldsymbol{x}_1)$–$[11\bar{2}](\boldsymbol{x}_2)$–$[\bar{1}10](\boldsymbol{x}_3)$ coordinate system due to the crystal orientation of our supercells. The coordinate system of reported elastic constants of Zr hydrides was changed (for the detail, please refer the appendix).

For comparison, we implemented the morphology prediction for two cases: *w/* and *w/o* the shear component of the calculated eigenstrain, because the existence of shear component of the eigenstrain for Zr hydrides is controversial issue recently [20,22,24,25,32]. For *w/o* shear case, as rough approximation, we simply set ϵ_{12} as zeros. The setting *w/o* shear component of the eigenstrain corresponds to the case in which the phase transformation pathway from HCP to FCT (or FCC), which was explained above, is not considered, or the case in

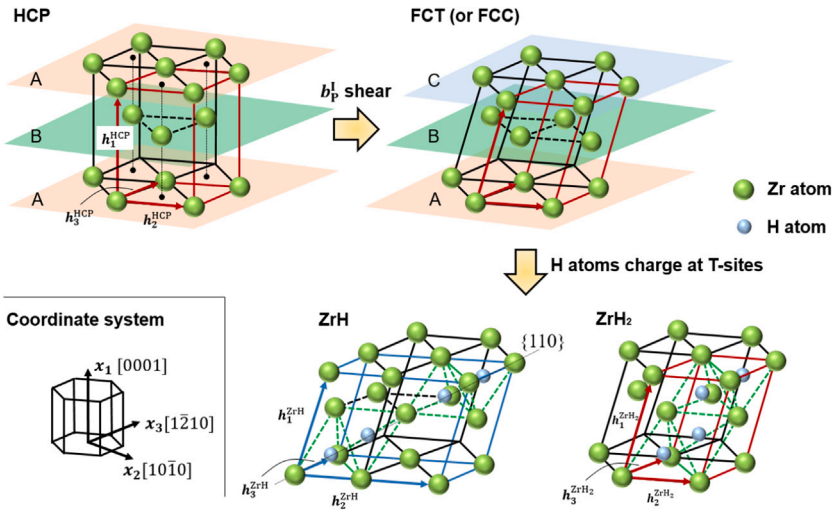

Fig. 3. Atomic structures of HCP Zr, FCT Zr, ZrH and ZrH_2 and these supercells used for atomic simulation with DFT calculation, which are shown by red and blue lines. H atoms were placed on the T-sites on the {110} plane and all T-sites of the FCT Zr structure for the most stable ZrH and ZrH_2 structures, respectively [6]. Green lines are guides for the eye to understand the position of the T-sites.

Table 1
Eigenstrains of ZrH, $ZrH_{1.66}$(interpolated) and ZrH_2 calculated using atomistic simulation with DFT calculation. Note $\epsilon_{ij} = \epsilon_{ji}$ and the values of other ϵ_{ij} not listed are zeros. For the comparison, the eigenstrain calculated using previous reported lattice constants are also included.

	ϵ_{11}	ϵ_{22}	ϵ_{33}	ϵ_{12}
ZrH				
This work	0.103	0.119	0.006	0.250
Expt [16]	0.057	0.050	0.010	0.183
DFT [28]	0.053	0.065	0.006	0.181
DFT [29]	0.057	0.068	0.002	0.181
DFT [30]	0.060	0.065	0.001	0.182
DFT [31]	0.055	0.062	0.007	0.181
$ZrH_{1.66}$				
This work	0.080	0.062	0.068	0.166
Expt [16]	0.073	0.046	0.046	0.190
DFT($ZrH_{1.5}$) [28]	0.042	0.025	0.025	0.184
DFT($ZrH_{1.5}$) [29]	0.067	0.044	0.044	0.188
DFT($ZrH_{1.5}$) [30]	0.072	0.045	0.045	0.189
DFT($ZrH_{1.5}$) [31]	0.066	0.047	0.047	0.189
ZrH_2				
This work	0.068	0.033	0.101	0.123
DFT [28]	0.017	−0.038	0.036	0.186
DFT [29]	0.077	0.012	0.096	0.198
DFT [30]	0.080	0.010	0.095	0.199
DFT [31]	0.076	0.015	0.095	0.197

which the shear component of the eigenstrain is released by subsequent plastic deformation (e.g., dislocation emission around the Zr hydride precipitate) or canceled out due to the mix of Shockley partials [20,32]. Generally, not only ϵ_{12}, other strain components also change due to the plastic deformation because HCP Zr matrix have multiple slip systems with different orientation. Despite of it, the above setting corresponds to consider a certain basal slip system reduces all shear components of the coordinate system as zero. We do not want to say this is real situation, it is a rough approximation. However, because HCP-FCT transformation causes a large basal shear ϵ_{12} as in Table 1, at first stage of the deformation, the plastic deformation will mainly occur on the slip system. As a suggestion for the further investigation, because we know the slip systems of HCP Zr matrix are basal, prismatic and pyramidal, changing the coordinate system of strain tensor using rotation matrix and iteratively removing the shear components of these slip systems from the strain tensor would be more convincing modeling.

3. Results and discussion

3.1. Morphology of Zr hydride precipitates under zero stress condition

In Table 3, the calculated energy increment $\Delta\tilde{E}$ of the sphere-shaped precipitates for each Zr hydride ($w/$ and w/o shear component of eigenstrain) are listed. In Fig. 4 ($w/$ shear) and 5 (w/o shear), we show that $\Delta\tilde{E}$ changes with respect to rotation angle ϕ and ψ. Continuous $\Delta\tilde{E}(\phi,\psi)$ maps were drawn by spline interpolation of the calculated discrete $\Delta\tilde{E}(\phi,\psi)$ data. Note raw data of the discrete $\Delta\tilde{E}(\phi,\psi)$ map is available as supplemental material. The predicted stable shapes and orientations for each Zr hydride precipitate, which have the minimum $\Delta\tilde{E}$, are listed in Table 4 ($w/$ shear) and Table 5 (w/o shear). Experimentally observed shapes and orientations of Zr hydride precipitates are also listed in Table 6. Fig. 6 is a schematic of the predicted stable shape and orientation for each Zr hydride precipitate in HCP Zr matrix.

For the $w/$ shear case, independent of the type of Zr hydride, the $\Delta\tilde{E}$ value is small and almost equal in the range ϕ = 20–80°, ψ = 90 for the disk case, as shown in Fig. 4, indicating the reorientation of Zr hydride precipitate is easily occur in this angle range. The disk shape, which is 20–30°, titled about the ⟨1$\bar{2}$10⟩-axis from the basal plane (0001), as shown in Fig. 6, have the minimum $\Delta\tilde{E}$ value. The tilt angle becomes slightly larger as the hydride goes from δ to ϵ. This is qualitatively consistent with the experimental observation for δ hydride ($ZrH_{1.66}$); disk shape precipitates on basal plane (0001) nucleate first and then a macroscopic "deck of card" structure with several tilts about the ⟨1$\bar{2}$10⟩-axis is constructed subsequently [1,2]. Although Han *et al.* reported similar result using phase field simulation recently, suggesting the origin is the anisotropy of chemical interfacial energy [22], our analysis suggests the elastic origin of it. This is consistent with the result of another recent phase field simulation by Heo *et al.* [23], which successfully observed "deck of cards" structure, considering elastic heterogeneity between HCP Zr matrix and δ hydride. Meanwhile, the disk shape prediction for γ hydride (ZrH) is inconsistent with the needle shape observed in experiments [7,8]. Another interesting result is that $ZrH_{1.66}$ has the minimum $\Delta\tilde{E}$ of all Zr hydrides in Table 4. We believe this is the reason for the frequent observation of δ hydride in the experiment [1]. Previous atomic simulation results with DFT calculation revealed that ZrH_2 is the most stable Zr hydride at 0 K, despite experimental observations [6]. Although the reason for this inconsistency is considered as a thermal effect, our results suggest that δ hydride may be elastically favored.

Table 2
Elastic constants of HCP Zr, ZrH, $ZrH_{1.66}$(interpolated) and ZrH_2 calculated using atomistic simulation with DFT calculation. Note $C_{ijkl} = C_{jikl} = C_{ijlk} = C_{klij}$ and the values of other C_{ijkl} not listed are zeros. The unit of the elastic constants is GPa. The elastic constants of ZrH, $ZrH_{1.66}$ and ZrH_2 are defined in $[111](\boldsymbol{x}_1) - [11\bar{2}](\boldsymbol{x}_2) - [\bar{1}10](\boldsymbol{x}_3)$ coordinate system. For the comparison, the elastic constants, that were reported in previous studies are also included.

	C_{1111}	C_{2222}	C_{3333}	C_{1122}	C_{1133}	C_{2233}	C_{2323}	C_{3131}	C_{1212}	C_{1112}	C_{2212}	C_{3312}	C_{2331}
HCP Zr													
This work	165	149	149	70	70	65	41	27	27	0	0	0	0
Expt [50]	173	155	155	65	65	67	45	36	36	0	0	0	0
DFT [28]	181	159	159	66	66			18	18	0	0	0	0
DFT [29]	168	148	148	69	69	62	43	25	25	0	0	0	0
DFT [30]	174	152	152	67	67	66	44	25	25	0	0	0	0
DFT [31]	177	151	151	68	68	64	44	30	30	0	0	0	0
ZrH													
This work	194	194	188	96	78	85	31	22	42	0	0	18	21
DFT [28]	195	195	187	86	72	81	36	24	47	0	0	17	24
DFT [29]	188	188	183	93	69	83	33	18	43	0	0	20	21
DFT [30]	189	192	181	95	80	87	31	20	44	0	0	14	22
DFT [31]	184	184	176	89	73	83	31	19	40	0	0	18	22
DFT [34]	187	187	175	89	77	73	23	28	41	0	0	21	23
$ZrH_{1.66}$													
This work	201	191	221	108	96	100	30	22	43	−14	−11	11	14
DFT($ZrH_{1.5}$) [28]	163	139	139	−23	−23	3	69	43	43	0	−36	36	36
DFT($ZrH_{1.5}$) [29]	215	201	201	77	77	85	55	43	43	0	−19	19	19
DFT($ZrH_{1.5}$) [30]	168	152	152	114	114	129	11	−5	−5	0	−23	23	23
DFT($ZrH_{1.5}$) [31]	165	148	148	103	103	121	14	−4	−4	0	−25	25	25
DFT($ZrH_{1.5}$) [34]	191	161	180	74	115	107	46	23	30	0	−29	−7	21
ZrH_2													
This work	204	190	238	114	105	107	30	22	44	−21	−16	7	10
DFT [28]	86	96	85	16	29	18	37	40	41	2	8	−11	−2
DFT [29]	188	160	214	116	104	107	22	14	34	−18	−11	3	8
DFT [30]	196	162	231	127	105	110	21	17	35	−23	−11	7	4
DFT [31]	191	159	218	114	96	103	23	14	36	−19	−13	7	9
DFT [34]	184	174	227	115	99	100	24	22	43	−20	−17	5	9

Table 3
Elastic energy increment $\Delta\tilde{E}$ of sphere-shaped Zr hydride precipitates.

Zr hydride	$\Delta\tilde{E}$ GJ/m^3 ($w/$ shear)	$\Delta\tilde{E}$ (w/o shear)
ZrH	3.71	1.06
$ZrH_{1.66}$	1.86	0.78
ZrH_2	1.33	0.79

Table 4
Shapes and orientations of Zr hydride precipitates with the minimum elastic energy increment ($w/$ shear).

Zr hydride	Shape/angle (ϕ, ψ)	$\Delta\tilde{E}$ GJ/m^3
ZrH	Disk/(20° or 70°, 90°)	0.99
$ZrH_{1.66}$	Disk/(20° or 60°, 90°)	0.72
ZrH_2	Disk/(30°, 90°)	0.86

Table 5
Shapes and orientations of Zr hydride precipitates with the minimum elastic energy increment (w/o shear).

Zr hydride	Shape/angle (ϕ, ψ)	$\Delta\tilde{E}$ GJ/m^3
ZrH	Needle/(0° to 180°, 0°)	0.72
$ZrH_{1.66}$	Disk/(160°, 50° or 130°)	0.57
ZrH_2	Disk/(160°, 40° or 140°)	0.48

For the w/o shear case, interestingly, the needle shape with ψ = 0°, which corresponds to the $[1\bar{2}10]$ longitudinal needle, consistent with experimental observations, is predicted to have a stable shape and orientation for ZrH hydride (γ hydride) precipitate, in contrast to $w/$ shear case. We think this is due to the dislocation emission around the Zr hydride precipitate [8,15–17]. Once dislocation emission occurs during the nucleation process of Zr hydrides, the shear strain due to HCP-FCT phase transformation may be released, and needle-shaped precipitates are chosen elastically. Thus, the morphology of the Zr hydride precipitates is correlated with the surrounding plastic deformation [21]. Note that for other Zr hydrides, the predicted stable disk tilted about $[10\bar{1}0]$-axis, as shown in Fig. 6, because ψ deviates largely from 90° in this case, which is inconsistent with experimental observation; to the best of our knowledge, disks tilted about the $\langle 10\bar{1}0\rangle$-axis have not been observed in experiment. As we mentioned, the existence of shear component of eigenstrain is controversial issue recently. From the consistency between our prediction and experimental observation, we think that the shear component of eigenstrain due to HCP to FCT (or FCC) phase transformation is necessary elastically because we cannot predict the deviated disk-shape correctly without the shear component using our method, but the shear strain may be released or canceled out owing to the subsequent plastic deformation or mixing of Shockley partials, which changes the morphology of the Zr hydride, producing the needle shape γ hydride.

3.2. Effect of external stress on the morphology of Zr hydride precipitates

Next, to study the effect of external stress $\sigma^{\mathrm{ex}}_{ij}$ on the morphology of the Zr hydride precipitate, we extract the $\sigma^{\mathrm{ex}}_{ij}$ term from Eq. (6) as

$$\Delta\tilde{E}_{\mathrm{ex}} \equiv -\sigma^{\mathrm{ex}}_{ij}\epsilon_{ij} - \frac{1}{2}\sigma^{\mathrm{ex}}_{ij}(\tilde{\epsilon}_{ij} - \epsilon_{ij}). \tag{11}$$

For each Zr hydride, we calculated the $\Delta\tilde{E}_{\mathrm{ex}}$ for a spherical precipitate, and the $\Delta\tilde{E}_{\mathrm{ex}}$ change with respect to the rotation angle ϕ and ψ for disk and needle precipitates. Here, $\sigma^{\mathrm{ex}}_{ij}$ is set as $\sigma^{\mathrm{ex}}_{22}$ = 1.0 GPa ($[10\bar{1}0]$ tension) or $\sigma^{\mathrm{ex}}_{33}$ = 1.0 GPa ($[1\bar{2}10]$ tension) and other components are zero, as it is consistent with the circumferential tensile stress on the basal plane (0001) in the experiment [1,2] and the eigenstrains of each Zr hydride are $w/$ shear because the disk shape of the δ hydride is well predicted using $w/$ shear eigenstrains as we mentioned in previous section. Note, for the unification, we use the eigenstrains $w/$ shear strain for ZrH though the morphology was well predicted for w/o shear case in previous section. Because the external stress effect is always discussed for the δ hydride, but not very interested for the γ hydride, we think this

Table 6
Experimentally observed shapes and orientations of Zr hydride precipitates.

Zr hydride	Shape/orientation
ZrH	Needle/$\langle 1\bar{2}10\rangle$ longitudinal [7,8]
$ZrH_{1.66}$ (nano-scale)	Disk/[0001] normal [4]
$ZrH_{1.66}$ (micro-scale)	"deck of cards" structure/[0001] normal, 14.7° tilted about $\langle 1\bar{2}10\rangle$ [51]

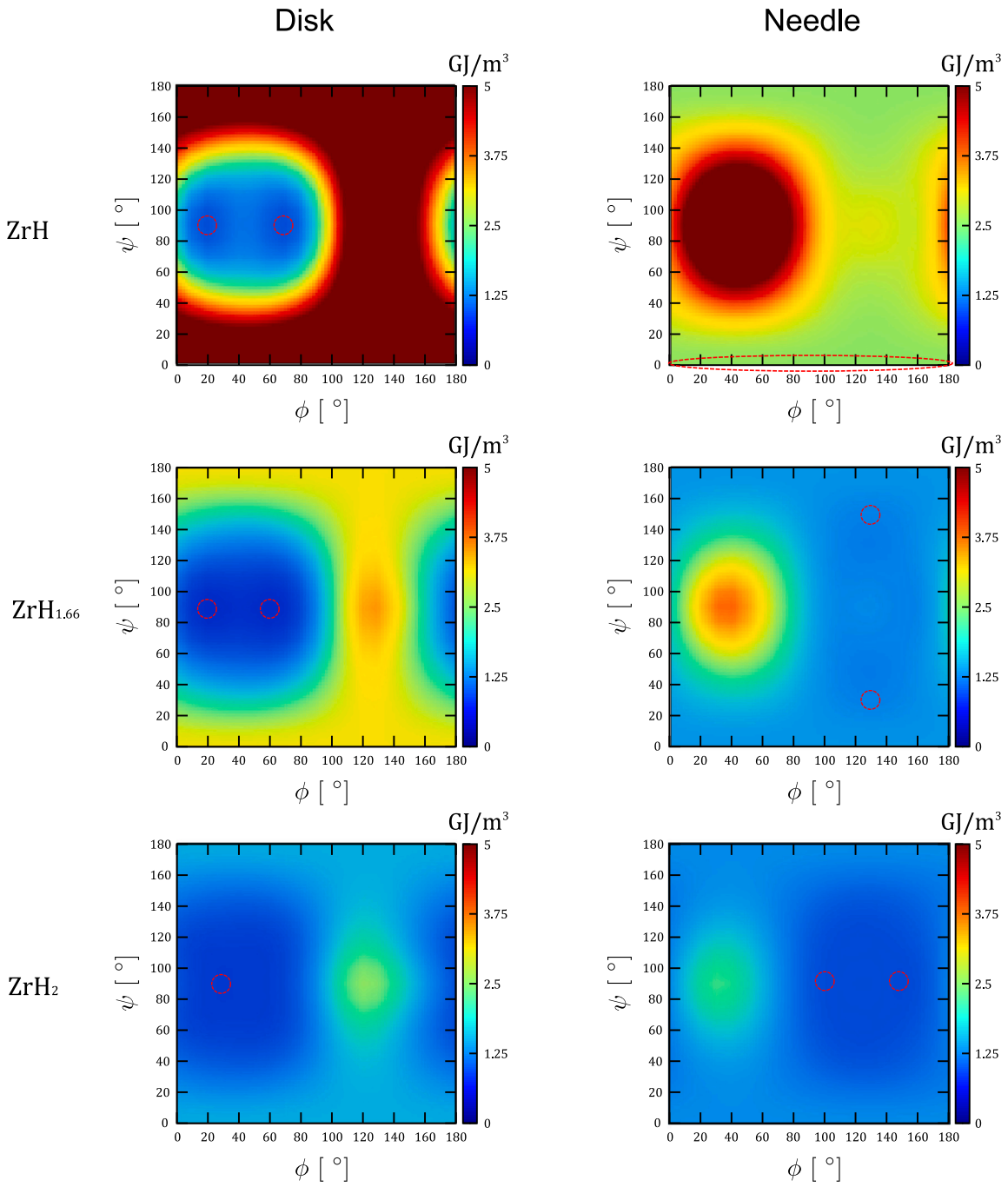

Fig. 4. Elastic energy increment $\Delta\tilde{E}$ change with respect to ϕ and ψ ($w/$ shear). Broken circles and ellipses indicate the area with the minimum $\Delta\tilde{E}$ for each case.

is not a big problem. In Table 7, the calculated energy increment $\Delta\tilde{E}_{ex}$ of the sphere-shaped precipitates for each Zr hydride ($[10\bar{1}0]$ and $[1\bar{2}10]$ tension) are listed. In Fig. 7 ($[10\bar{1}0]$ tension) and 8 ($[1\bar{2}10]$ tension), we show the $\Delta\tilde{E}_{ex}$ change with respect to rotation angles ϕ and ψ. The shapes and orientations of each Zr hydride precipitate, which has the minimum $\Delta\tilde{E}_{ex}$, are listed in Table 8 ($[10\bar{1}0]$ tension) and Table 9 ($[1\bar{2}10]$ tension). Fig. 9 is a schematic of the predicted stable shape and orientation (with the minimum value of $\Delta\tilde{E}_{ex}$) for each Zr hydride precipitate in HCP Zr matrix under external stress condition.

From Fig. 7 and Table 8, the $[10\bar{1}0]$ tensile stress mainly stabilizes the needle shape. Regarding the orientation, it primarily stabilizes the disk tilted about the $[10\bar{1}0]$-axis and the $[10\bar{1}0]$ longitudinal needle for ZrH, the [0001] parallel disk (prismatic plane $(10\bar{1}0)$ normal) and [0001] longitudinal needle for $ZrH_{1.66}$ and ZrH_2. In contrast, the $[1\bar{2}10]$ tensile

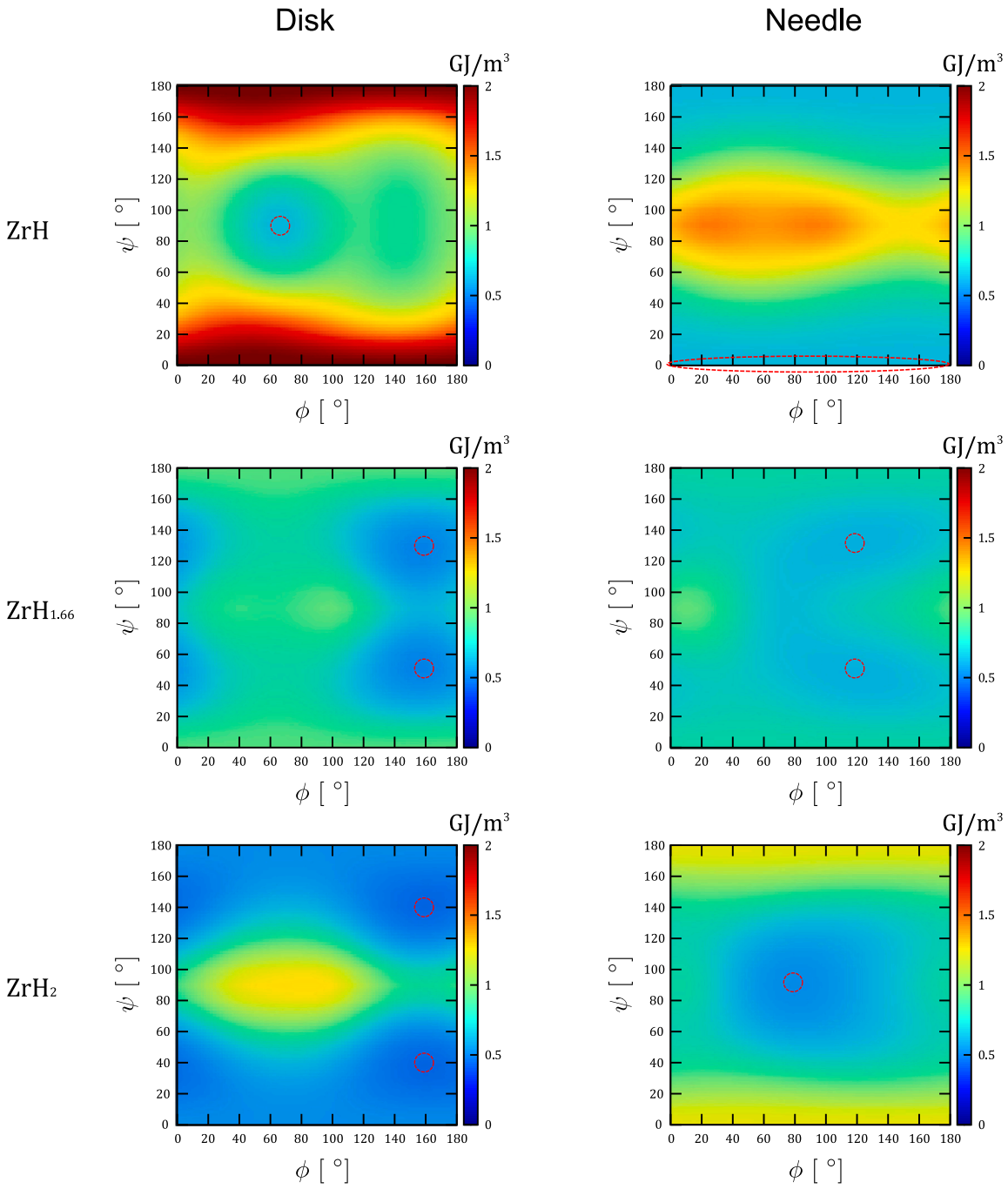

Fig. 5. Elastic energy increment $\Delta\tilde{E}$ change with respect to ϕ and ψ (w/o shear). Broken circles and ellipses indicate the area with the minimum $\Delta\tilde{E}$ for each case.

Table 7
$\Delta\tilde{E}_{ex}$ of sphere-shaped Zr hydride precipitates under 1.0 GPa tensile stress.

Zr hydride	$\Delta\tilde{E}_{ex}$ GJ/m^3 ($[10\bar{1}0]$ tension)	$\Delta\tilde{E}_{ex}$ ($[1\bar{2}10]$ tension)
ZrH	−0.12	8.0×10^{-4}
$ZrH_{1.66}$	−0.059	−0.066
ZrH_2	−0.028	−0.10

Table 8
Shapes and orientations of Zr hydride precipitates with the minimum $\Delta\tilde{E}_{ex}$ under 1.0 GPa tensile stress along $[10\bar{1}0]$.

Zr hydride	Shape/angle (ϕ,ψ)	$\Delta\tilde{E}_{ex}$ GJ/m^3
ZrH	Needle/(70°, 90°)	−0.13
$ZrH_{1.66}$	Needle/(0°, 90°)	−0.063
ZrH_2	Needle/(0°, 90°)	−0.034

stress mainly stabilizes the disk shape, as shown in Fig. 8 and Table 9. It stabilizes the disk tilted about both the $[10\bar{1}0]$- and $[1\bar{2}10]$-axis and $[1\bar{2}10]$ longitudinal needle slightly tilted about the $[10\bar{1}0]$- and [0001]-axis for ZrH, the [0001] parallel disk (prismatic plane $(10\bar{1}0)$ normal) and $[1\bar{2}10]$ longitudinal needles for the $ZrH_{1.66}$ and ZrH_2. The prediction of the [0001] parallel disk of the $ZrH_{1.66}$ precipitate is consistent with experimental observations of the reorientation of δ hydride cluster in the radial direction during cooling under circumferential tensile stress conditions [1,2,4]. However, from the comparison of the magnitudes

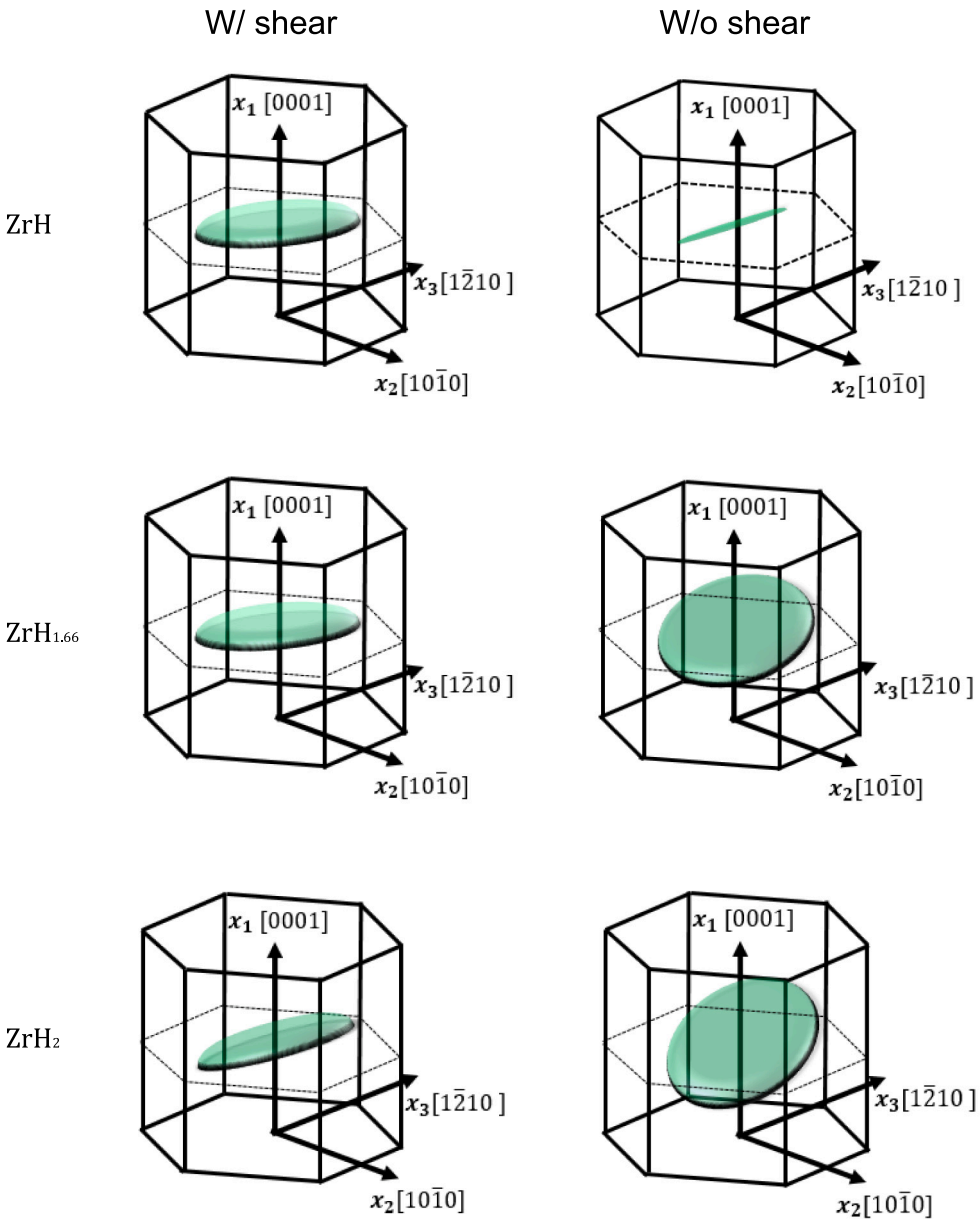

Fig. 6. Schematic of the predicted stable shape and orientation for ZrH, $ZrH_{1.66}$ and ZrH_2. Needle shape was predicted for ZrH (ω/o) and tilted disks from basal plane were predicted for others.

of the $\Delta\tilde{E}$ and $\Delta\tilde{E}_{ex}$, we must note that the effect of external stress on the morphology of Zr hydride precipitates is not significant; $\frac{1}{2}\sigma_{ij}\epsilon_{ij}$ in Eq. (6) is much larger than $\Delta\tilde{E}_{ex}$ under 1.0 GPa external stress. We confirmed that a [1$\bar{2}$10] tensile stress on the order of 10 GPa is necessary in our analysis for the reorientation of the $ZrH_{1.66}$ disk from [0001] normal to parallel: $\Delta\tilde{E} \approx \Delta\tilde{E}_{ex}$, which is quite large compared with the experimental critical tensile stress for the reorientation of several hundred MPa [52,53]. This is because the effect of elastic heterogeneity, $\tilde{\epsilon}_{ij} - \epsilon_{ij}$, is relatively small. About the reason of this, further investigation is still necessary.

Additionally, for the calculated $\Delta\tilde{E}_{ex}$ value, the [10$\bar{1}$0] tensile stress has a relatively low effect on the morphology of ZrH_2 (the minimum value is just −0.034 GJ/m^3 from Table 8) compared with ZrH and ZrH_2. This is because of the inconsistency between the direction of the tensile stress and the normal eigenstrain component; the eigenstrain of ZrH_2 has a very small [10$\bar{1}$0] normal strain component, ϵ_{22}, compared with other components from Table 1. When external stress is applied to the distorted direction by the eigenstrain, some of the internal distortion caused by the eigenstrain is released by the external stress because Zr hydride precipitates are stiffer than HCP Zr matrix (see Table 2), reducing the elastic energy caused by the precipitate and affecting the morphology of the precipitate. The same is true for the low effect of the [1$\bar{2}$10] tensile stress on ZrH.

Table 9
Shapes and orientations of Zr hydride precipitates with the minimum $\Delta\tilde{E}_{ex}$ under 1.0 GPa tensile stress along [1$\bar{2}$10].

Zr hydride	Shape/angle (ϕ, ψ)	$\Delta\tilde{E}_{ex}$ GJ/m^3
ZrH	Disk/(50°, 60° or 120°)	-9.1×10^{-3}
$ZrH_{1.66}$	Disk/(80°, 90°)	−0.079
ZrH_2	Disk/(80°, 90°)	−0.12

4. Summary

In summary, considering Zr hydride precipitates as ellipsoids, we energetically predicted the morphology of Zr hydride precipitates (γ,

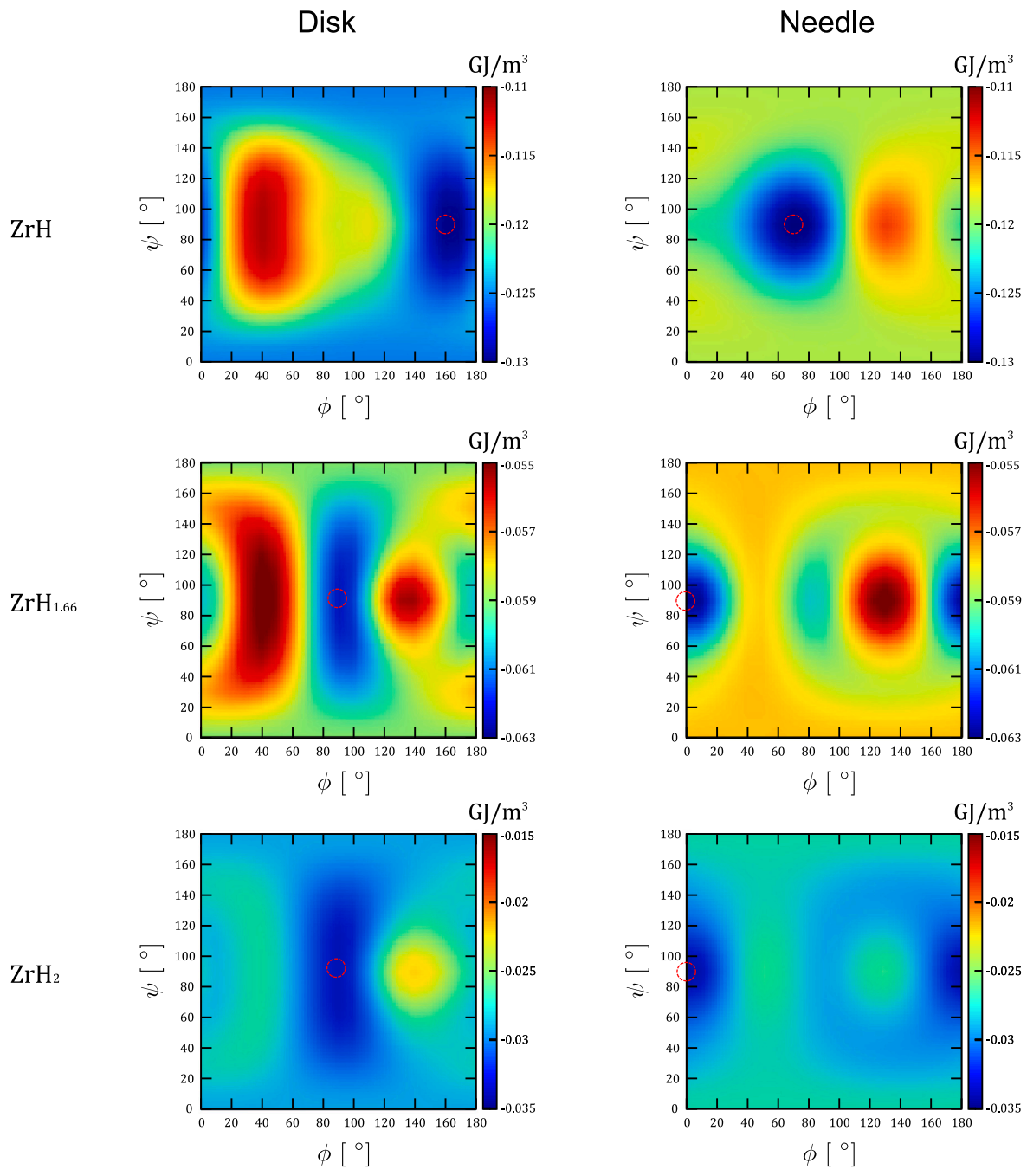

Fig. 7. Elastic energy increment $\Delta\tilde{E}_{ex}$ change with respect to ϕ and ψ under 1.0 GPa tensile stress along $[10\bar{1}0]$. The broken circles indicate the area with the minimum $\Delta\tilde{E}_{ex}$ for each case.

δ, and ϵ) in the HCP Zr matrix using Eshelby's ellipsoidal inclusions to calculate the elastic energy increment due to the presence of Zr hydride precipitates in the Zr matrix, where the elastic anisotropy and inhomogeneity of the elastic constants between Zr matrix and Zr hydrides are considered. As candidates of the shape, plates (mimicked by penny-shape ellipsoids), needles (mimicked by longitudinal ellipsoids) and sphere were employed. The stable shape and orientation of the Zr hydride precipitates were detected by comparing the difference in the elastic energy increment between the ellipsoidal inclusions with different shapes and orientations. The eigenstrains of each Zr hydride and the elastic constants of Zr hydrides and Zr matrix for Eshelby's ellipsoidal inclusion analysis were determined using atomistic simulation with a DFT calculation, achieving a parameter free *ab initio* morphology prediction. The morphology predictions were implemented for two cases: with and without shear components of eigenstrain ($w/$ and w/o shear).

As a result, the $\langle 1\bar{2}10\rangle$ longitudinal needle (w/o shear) for the γ hydride and plate (or disk) on the plane, which is 20° to 30° tilted about $\langle 1\bar{2}10\rangle$-axis from the basal plane (0001), for δ and ϵ hydrides ($w/$ shear), are predicted to have a stable shape and orientation under zero external stress conditions, which is qualitatively consistent with experimental observations. The external circumferential tensile stress on the basal plane reduces the elastic energy of the [0001] parallel Zr hydride plates, which is also qualitatively consistent with the reoriented δ hydride precipitates observed in the experiment. Generally, our predictions based on elasticity theory are qualitatively consistent with experimental observations, suggesting an elastic origin of the morphology of Zr hydride in the HCP Zr matrix. Additionally, we

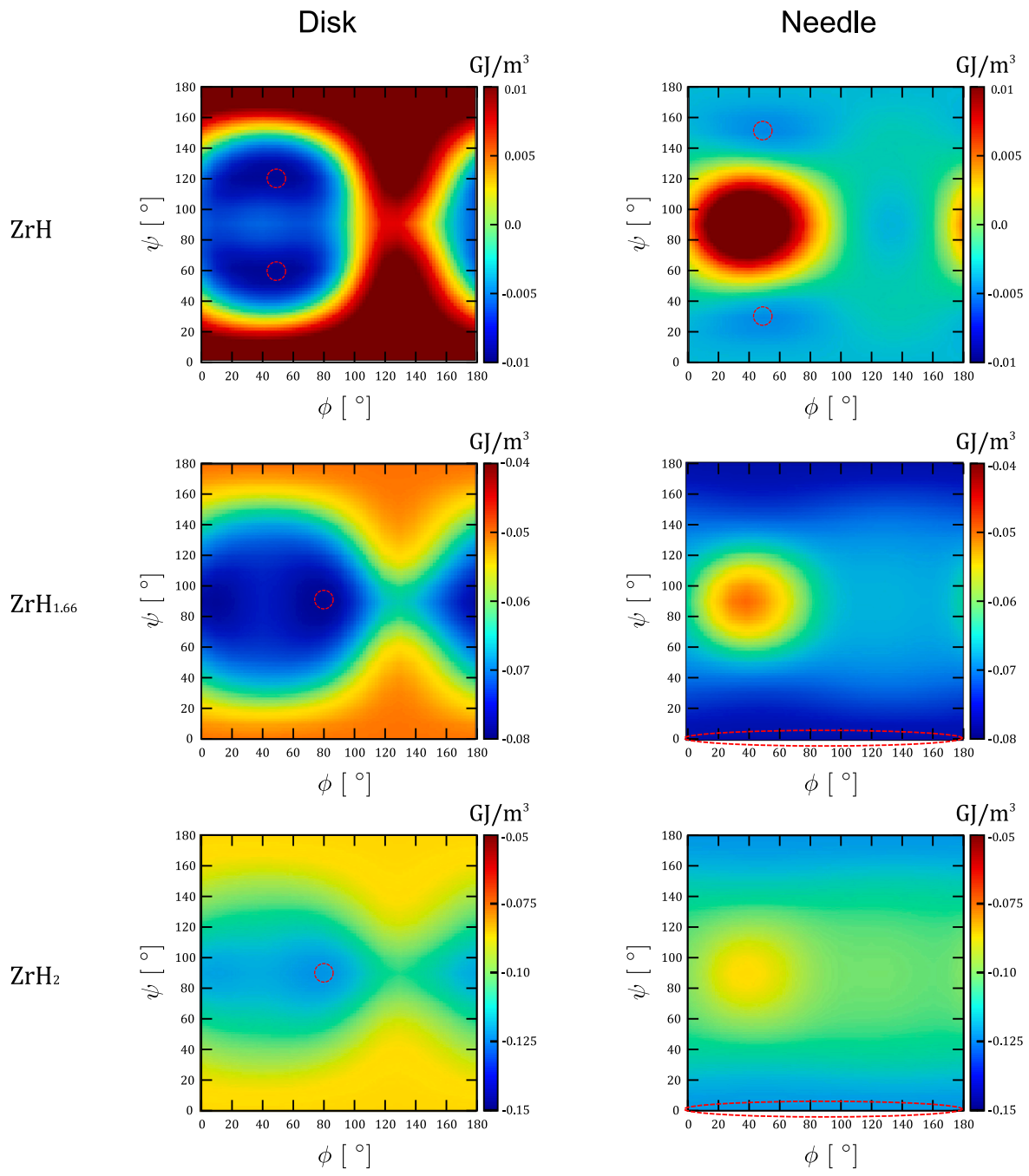

Fig. 8. Elastic energy increment $\Delta\tilde{E}_{ex}$ change with respect to ϕ and ψ under 1.0 GPa tensile stress along $[1\bar{2}10]$. Broken circles and ellipses indicate the area with the minimum $\Delta\tilde{E}_{ex}$ for each case.

have to mention that our approach is applicable for the morphology prediction of secondary phase in solid materials generally. E.g., the morphology of martensite in austenite for conventional steel will be one of targets of our analysis.

Finally, we should mention that further improvement of our method is still necessary for the practical quantitative prediction despite the above qualitative success of the morphology prediction. Predicted external stress for the reorientation of Zr hydride is quite high, around 10 GPa. This is inconsistent with experimental observation and further investigation is necessary. Not only the chemical interface energy, we need to consider the effects of temperature and the plastic deformation of inside/outside of Zr hydrides too. One can include thermal effects in Eshelby's ellipsoidal inclusions as temperature-dependent elastic constants and thermal strains due to the difference of thermal expansion between inclusion and matrix in eigenstrains. Phonon analysis using DFT calculation will achieve *ab initio* calculation of temperature-dependent elastic constants and the thermal strains [54, 55]. Bowles–Mackenzie or Wechsler–Lieberman–Read phenomenological theory [56] will be an useful parameter-free approach to consider the effect of the plastic deformation of the inside of Zr hydrides, assuming the existence of zero strain plane in the hydrides though the analysis is no more *ab initio*. Because the intermediate shape between disks and spheres was observed recently using phase-field method [25] and "the deck of cards" structure spans over several grains [1], further investigations for the shapes of Zr hydrides and the effect of multiple grains to "the deck of cards" structure are also necessary, changing

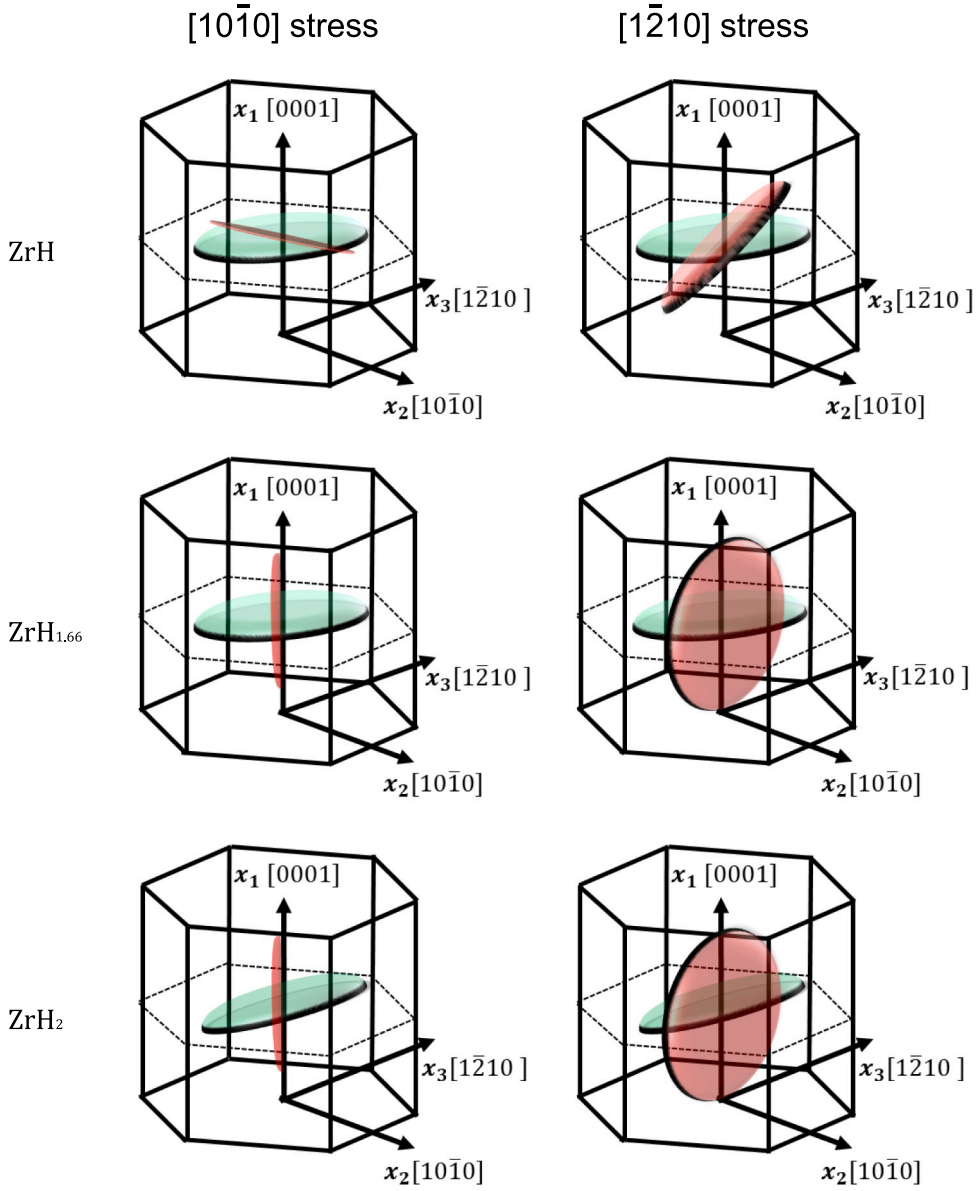

Fig. 9. Schematic of the predicted stable shape and orientation (with the minimum value of $\Delta\tilde{E}_{ex}$) for ZrH, $ZrH_{1.66}$ and ZrH_2 under external stress condition (red inclusions). The predicted shapes without external stress are also shown as references (green inclusion). As most stabilized shapes by the stress, the needle shapes were predicted under [10$\bar{1}$0] stress and [0001] parallel disks were predicted under [1$\bar{2}$10] stress.

the diameters of ellipsoid, a_1, a_2 and a_3, and the elastic constants to grains-averaged ones.

CRediT authorship contribution statement

Akio Ishii: Conceptualization, Methodology, Validation, Investigation, Writing – original draft, Writing – review & editing, Visualization, Funding acquisition.

Declaration of competing interest

The authors declare that they have no known competing financial interests or personal relationships that could have appeared to influence the work reported in this paper.

Acknowledgments

This study was partially supported by a Grant-in-Aid for Early Career Scientists 18K13658 and Grant-in-Aid for Scientific Research (C) 21K03771 from Japan Society for the Promotion of Science (JSPS). DFT calculations were partly carried out using the OCTOPUS large-scale computer systems at the Cybermedia Center, Osaka University.

Appendix A. Calculation of the eigenstrains and the rotation matrix using lattice constants of HCP and FCT

From the lattice correspondence between HCP and FCT (please see Fig. A.1), the eigenstrains of previous studies in Table 1 were calculated using reported lattice constants of HCP Zr, a_{HCP} and c_{HCP}, and those of Zr hydride, a_{ZrH_x} and c_{ZrH_x} as

$$\epsilon_{11} = \frac{1}{c_{HCP}}\left(\frac{2}{3}\sqrt{2a_{ZrH_x}^2 + c_{ZrH_x}^2} - c_{HCP}\right),$$

$$\epsilon_{22} = \frac{1}{\sqrt{3}a_{HCP}}\left(\frac{1}{2}\sqrt{2a_{ZrH_x}^2 + 4c_{ZrH_x}^2} - \sqrt{3}a_{HCP}\right),$$

$$\epsilon_{33} = \frac{1}{a_{HCP}}\left(\frac{a_{ZrH_x}}{\sqrt{2}} - a_{HCP}\right),$$

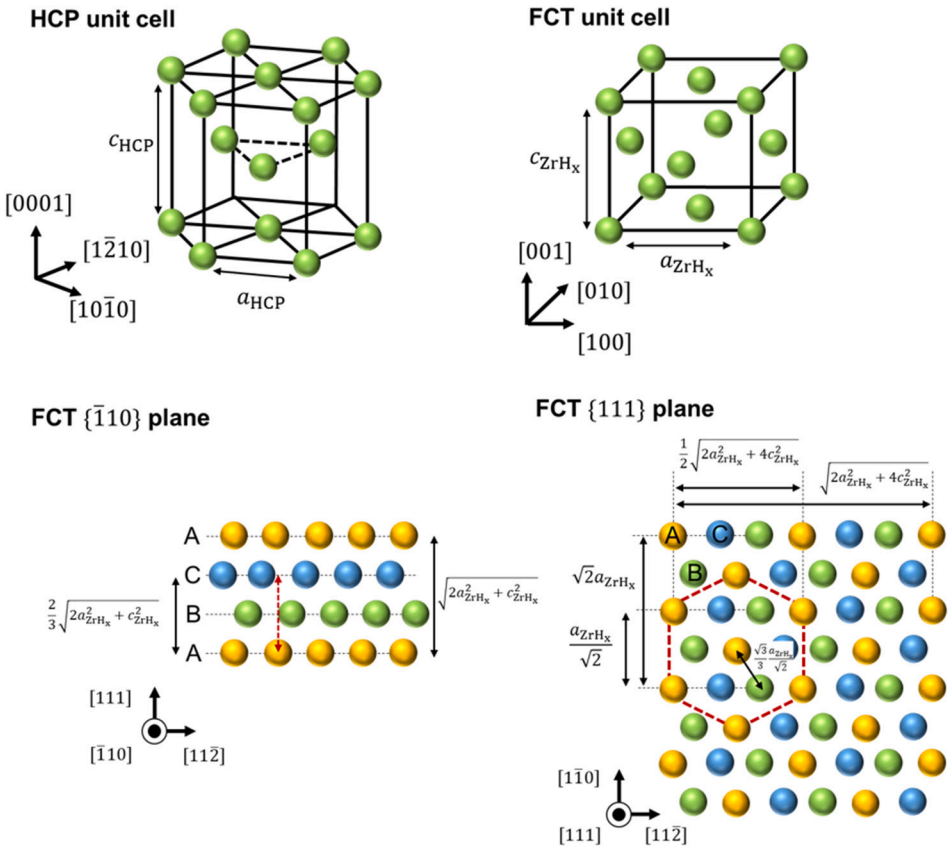

Fig. A.1. Atomic structures of HCP and FCT. The red broken arrow in FCT {1$\bar{1}$0} plane (left bottom) and red broken line in FCT {111} plane (right bottom) indicate the corresponding height and basal unit of HCP unit cell, respectively.

$$\epsilon_{12} = \frac{1}{2}\left(\frac{1}{c_{HCP}}\frac{\sqrt{3}}{3}\frac{a_{ZrH_x}}{\sqrt{2}}\right).$$

In Table 2, the coordinate system of Zr hydrides' elastic constants of previous studies is changed to that of our study: [111]($\boldsymbol{x}_1$)−[11$\bar{2}$]($\boldsymbol{x}_2$)−[$\bar{1}$10]($\boldsymbol{x}_3$), corresponding [0001] – [10$\bar{1}$0] – [12$\bar{1}$0] of HCP Zr matrix, using the following rotation matrix R^{ela}_{ij},

$$\boldsymbol{r}_{x_1} = \begin{bmatrix} \frac{a_{ZrH_x}}{\sqrt{2a^2_{ZrH_x}+c^2_{ZrH_x}}} \\ \frac{a_{ZrH_x}}{\sqrt{2a^2_{ZrH_x}+c^2_{ZrH_x}}} \\ \frac{c_{ZrH_x}}{\sqrt{2a^2_{ZrH_x}+c^2_{ZrH_x}}} \end{bmatrix},$$

$$\boldsymbol{r}_{x_3} = \begin{bmatrix} \frac{-1}{\sqrt{2}} \\ \frac{1}{\sqrt{2}} \\ 0 \end{bmatrix},$$

$$\boldsymbol{r}_{x_2} = \frac{\boldsymbol{r}_{x_1}\times\boldsymbol{r}_{x_2}}{|\boldsymbol{r}_{x_1}\times\boldsymbol{r}_{x_2}|},$$

$$R^{ela}_{ij} \equiv [\boldsymbol{r}_{x_1}\ \boldsymbol{r}_{x_2}\ \boldsymbol{r}_{x_3}].$$

Appendix B. Supplementary data

Supplementary material related to this article can be found online at https://doi.org/10.1016/j.commatsci.2022.111500.

References

[1] A.T. Motta, L. Capolungo, L.Q. Chen, M.N. Cinbiz, M.R. Daymond, D.A. Koss, E. Lacroix, G. Pastore, P.C.A. Simon, M.R. Tonks, B.D. Wirth, M.A. Zikry, Hydrogen in zirconium alloys: A review, J. Nucl. Mater. 518 (2019) 440–460.
[2] A.A. Plyasov, V.V. Novikov, Y.N. Devyatko, A review of hydride reorientation in zirconium alloys for water-cooled reactors, Phys. Atom. Nucl. 83 (2020) 1407–1424.
[3] D.O. Northwoodkosasih, Hydrides and delayed hydrogen cracking in zirconium and its alloys, Intell. Met. Rev. 28 (1983) 92–121.
[4] C.E. Ells, Hydride precipitates in zirconium alloys (A review), J. Nucl. Mater. 28 (1968) 129–151.
[5] J. Bair, M. Asle Zaeem, M. Tonks, A review on hydride precipitation in zirconium alloys, J. Nucl. Mater. 466 (2015) 12–20.
[6] M. Christensen, W. Wolf, C. Freeman, E. Wimmer, R.B. Adamson, L. Hallstadius, P.E. Cantonwine, E.V. Mader, H in -Zr and in zirconium hydrides: Solubility, effect on dimensional changes, and role of defects, J. Phys. Condens. Matter 27 (2015) 025402.
[7] G.J. Carpenter, J.F. Watters, An in situ study of the dissolution of γ-zirconium hydride in zirconium, J. Nucl. Mater. 73 (1978) 190–197.
[8] S.-M. Liu, A. Ishii, S.-B. Mi, S. Ogata, J. Li, W. Han, Dislocation-mediated hydride precipitation in zirconium, Small 2105881 (2021) 1–8.
[9] K. Sakamoto, M. Nakatsuka, Stress reorientation of hydrides in recrystallized zircaloy-2 sheet, J. Nucl. Sci. Technol. 43 (2006) 1136–1141.
[10] S.-J. Min, M.-S. Kim, K.-T. Kim, Cooling rate- and hydrogen-content-dependent hydride reorientation and mechanical property degradation of Zr-Nb alloy claddings, J. Nucl. Mater. 441 (2013) 306–314.
[11] J.-M. Lee, H.-A. Kim, D.-H. Kook, Y.-S. Kim, A study on the effects of hydrogen content and peak temperature on threshold stress for hydride reorientation in Zircaloy-4 cladding, J. Nucl. Mater. 509 (2018) 285–294.
[12] J.S. Kim, T.H. Kim, D.-H. Kook, Y.S. Kim, Effects of hydride morphology on the embrittlement of Zircaloy-4 cladding, J. Nucl. Mater. 456 (2015) 235–245.
[13] R.K. Sharma, S. Sunil, B. Kumawat, R. Singh, A. Tewari, B. Kashyap, Influence of hydride orientation on fracture toughness of CWSR Zr-2.5% Nb pressure tube material between RT and 300 °C, J. Nucl. Mater. 488 (2017) 231–244.
[14] R.K. Sharma, A. Bind, G. Avinash, R. Singh, A. Tewari, B. Kashyap, Effect of radial hydride fraction on fracture toughness of CWSR Zr-2.5% Nb pressure tube material between the ambient and 300 °C temperatures, J. Nucl. Mater. 508 (2018) 546–555.
[15] J.E. Bailey, Electron microscope observations on the precipitation of zirconium hydride in zirconium, Acta Metall. 11 (1963) 267–280.
[16] J. Bradbrook, G. Lorimer, N. Ridley, The precipitation of zirconium hydride in zirconium and zircaloy-2, J. Nucl. Mater. 42 (1972) 142–160.

[17] G.J. Carpenter, J.F. Watters, R.W. Gilbert, Dislocations generated by zirconium hydride precipitates in zirconium and some of its alloys, J. Nucl. Mater. 48 (1973) 267–276.

[18] V. Perovic, G.R. Purdy, L.M. Brown, On the stability of arrays of precipitates, Acta Metall. 27 (1979) 1075–1084.

[19] V. Perovic, G. Weatherly, C. Simpson, Hydride precipitation in α/β zirconium alloys, Acta Metall. 31 (1986) 1381–1391.

[20] M.-A. Louchez, L. Thuinet, R. Besson, A. Legris, Microscopic phase-field modeling of hcp|fcc interfaces, Comput. Mater. Sci. 132 (2017) 62–73.

[21] H. Tummala, L. Capolungo, C.N. Tomé, Quantifying the stress state in the vicinity of a δ-hydride in α-zirconium, J. Nucl. Mater. 511 (2018) 406–416.

[22] G. Han, Y. Zhao, C. Zhou, D.-Y. Lin, X. Zhu, J. Zhang, S. Hu, H. Song, Phase-field modeling of stacking structure formation and transition of δ-hydride precipitates in zirconium, Acta Mater. 165 (2019) 528–546.

[23] T.W. Heo, K.B. Colas, A.T. Motta, L.-Q. Chen, A phase-field model for hydride formation in polycrystalline metals: Application to δ-hydride in zirconium alloys, 181 (2019) 262–277.

[24] I.A. Khan, A.C. Cocks, J. Chattopadhyay, A study of hydride precipitation in zirconium, Mech. Mater. 155 (2021) 103773.

[25] P.-C. Simon, L.K. Aagesen, A.M. Jokisaari, L.-Q. Chen, M.R. Daymond, A.T. Motta, M.R. Tonks, Investigation of δ zirconium hydride morphology in a single crystal using quantitative phase field simulations supported by experiments, J. Nucl. Mater. 557 (2021) 153303.

[26] A. Ishii, Energetics of heterogeneous Mg $\{10\bar{1}2\}$ deformation twinning migration using an atomistically informed phase-field model, Comput. Mater. Sci. 183 (2020) 109907.

[27] C. Domain, R. Besson, A. Legris, Atomic-scale Ab-initio study of Zr-H system: I. Bulk properties, Acta Mater. 50 (2002) 3513–3526.

[28] W. Zhu, R. Wang, G. Shu, P. Wu, H. Xiao, First-principles study of different polymorphs of crystalline zirconium hydride, J. Phys. Chem. C 114 (2010) 22361–22368.

[29] P. Olsson, A. Massih, J. Blomqvist, A.-M. Alvarez Holston, C. Bjerkén, Ab initio thermodynamics of zirconium hydrides and deuterides, Comput. Mater. Sci. 86 (2014) 211–222.

[30] P.F. Weck, E. Kim, V. Tikare, J.A. Mitchell, Mechanical properties of zirconium alloys and zirconium hydrides predicted from density functional perturbation theory, Dalton Trans. 44 (2015) 18769–18779.

[31] J. Zheng, X. Zhou, L. Mao, H. Zhang, J. Liang, L. Sheng, S. Peng, First-principles study of the relative stability of various zirconium hydrides using the special quasirandom structures approach, Inter. J. Hydrog. Energy 40 (2015) 4597–4604.

[32] Y. Zhang, X.M. Bai, J. Yu, M.R. Tonks, M.J. Noordhoek, S.R. Phillpot, Homogeneous hydride formation path in α-Zr: molecular dynamics simulations with charge-optimized many-body potentials, Acta Mater. 111 (2016) 357–365.

[33] Y. Zhang, C. Jiang, X. Bai, Anisotropic hydrogen diffusion in α-Zr and Zircaloy predicted by accelerated kinetic Monte Carlo simulations, Sci. Rep. 7 (2017) 41033.

[34] X. Zhu, D.Y. Lin, J. Fang, X.Y. Gao, Y.F. Zhao, H.F. Song, Structure and thermodynamic properties of zirconium hydrides by structure search method and first-principles calculations, Comput. Mater. Sci. 150 (2018) 77–85.

[35] T. Mura, Micromechanics of Defects in Solids, Springer Science & Business Media, 2013.

[36] Y. Wang, J. Li, Phase field modeling of defects and deformation, Acta Mater. 58 (2010) 1212–1235.

[37] P. Zhao, C. Shen, J. Li, Y. Wang, Effect of nonlinear and noncollinear transformation strain pathways in phase-field modeling of nucleation and growth during the martensite transformation, npj Comput. Mater. 3 (2017) 19.

[38] J.D. Eshelby, The determination of the elastic field of an ellipsoidal inclusion and related problems, Proc. R. Soc. Lond. Ser. A Math. Phys. Eng. Sci. 241 (1957) 376–396.

[39] J.D. Eshelby, Elastic inclusions and inhomogeneities, Prog. Solid Mech. 2 (1961) 89–140.

[40] N. Kinoshita, T. Mura, Elastic fields of inclusions in anisotropic media, Phys. Status Solidi (A) 5 (1971) 759–768.

[41] M. Kato, T. Fujii, S. Onaka, Elastic strain energies of sphere, plate and needle inclusions, Mater. Sci. Eng. A 211 (1996) 95–103.

[42] P. Zhao, J. Li, Y. Wang, Heterogeneously randomized STZ model of metallic glasses: Softening and extreme value statistics during deformation, Int. J. Plast. 40 (2013) 1–22.

[43] P. Zhao, J. Li, Y. Wang, Extended defects, ideal strength and actual strengths of finite-sized metallic glasses, Acta Mater. 73 (2014) 149–166.

[44] G. Kresse, J. Furthmüller, Efficient iterative schemes for ab initio total-energy calculations using a plane-wave basis set, Phys. Rev. B 54 (1996) 11169–11186.

[45] G. Kresse, D. Joubert, From ultrasoft pseudopotentials to the projector augmented-wave method, Phys. Rev. B 59 (1999) 11–19.

[46] J. Perdew, J. Chevary, S. Vosko, Atoms, molecules, solids, and surfaces applications of the generalized gradient approximation for exchange and correlation, Phys. Rev. B 46 (1992) 6671–6687.

[47] G.J. Carpenter, The dilatational misfit of zirconium hydrides precipitated in zirconium, J. Nucl. Mater. 48 (1973) 264–266.

[48] Y. Le Page, P. Saxe, Symmetry-general least-squares extraction of elastic data for strained materials from *abinitio* calculations of stress, Phys. Rev. B 65 (2002) 104104.

[49] X. Wu, D. Vanderbilt, D.R. Hamann, Systematic treatment of displacements, strains, and electric fields in density-functional perturbation theory, Phys. Rev. B 72 (2005) 1–13.

[50] E.S. Fisher, C.J. Renken, Single-crystal elastic moduli and the hcp → bcc transformation in Ti, Zr, and Hf, Phys. Rev. 135 (1964) A482–A494.

[51] H.M. Chung, R.S. Daum, J.M. Hiller, M.C. Billone, Characteristics of hydride precipitation and reorientation in spent-fuel cladding, in: Zirconium in the Nuclear Industry: Thirteenth International Symposium, ASTM STP-1423, 2002, pp. 561–582.

[52] M. Leger, A. Donner, The effect of stress on orientation of hydrides in zirconium alloy pressure-tube materials, Can. Metall. Q. 24 (1985) 235–243.

[53] M.N. Cinbiz, D.A. Koss, A.T. Motta, Influence of stress state on the reorientation of hydrides in a zirconium alloy, J. Nucl. Mater. 477 (2016) 157–164.

[54] U. Argaman, G. Makov, First-principles study of the temperature dependence of the elastic constants of hcp titanium, Comput. Mater. Sci. 184 (2020) 109917.

[55] G. Liu, J. Zhou, H. Wang, Anisotropic thermal expansion of SnSe from first-principles calculations based on Grüneisen's theory, Phys. Chem. Chem. Phys. 19 (2017) 15187–15193.

[56] C.M. Wayman, Introduction to the Crystallography of Martensitic Transformation, Macmillan, 1964.